

Far-Field Sensitivity to Local Boundary Perturbations in 2D Wave Scattering

Erik García Neefjes^{1*}, Stuart C. Hawkins¹

¹ School of Mathematical and Physical Sciences, Macquarie University, Sydney NSW 2109, Australia

March 14, 2025

Abstract

We numerically investigate the sensitivity of the scattered wave field to perturbations in the shape of a scattering body illuminated by an incident plane wave. This study is motivated by recent work on the inverse problem of reconstructing a scatterer shape from measurements of the scattered wave at large distances from the scatterer. For this purpose we consider star-shaped scatterers represented using cubic splines, and our approach is based on a Nyström method-based discretisation of the shape derivative. Using the singular value decomposition, we identify fundamental geometric modes that most strongly influence the scattered wave, providing insight into the most visible boundary features in scattering data.

Contents

1	Introduction	2
2	Scatterer representation: splines	3
3	Scattering model for sensitivity analysis	4
4	Numerical results	6
5	Conclusions	10

*Author for correspondence. E-mail: erik.garcia@mq.edu.au

1 Introduction

When a wave interacts with a *scatterer*, its properties are modified through a process known as *wave scattering* [1]. The scattered wave pattern depends strongly on the shape and properties of the scatterer and the direction from which the wave approaches. Of particular interest is the response of the scattered wave at large distances from the scatterer, commonly known as the *far-field*. In this region, the scattered wave approximates an outgoing spherical wave, with its amplitude decreasing inversely with distance from the scatterer. Far-field patterns are important in practice since often measurements must be made at considerable distances from the scattering object. Given far-field measurements, reconstructing properties of the scatterer is a classical *ill-posed* inverse problem. While, consequently, the forward map from scatterers to far-fields has no inverse, various methods including iterative, qualitative, and regularization approaches have been developed to obtain useful approximate solutions [2].

For the inverse shape problem, remarkable reconstructions have been obtained with (deterministic) regularized Newton-type methods [7], as well as (stochastic) Bayesian counterparts [9]. In tackling this problem, following our work in [6], we noticed some interesting phenomena related to how well certain kinds of scatterer-dependent features can be reconstructed. In this paper, we aim to investigate these phenomena further by considering the forward problem for an illustrative geometry, and show how our previous observations can be explained via analysis of the shape-derivative. Interpreting this derivative is facilitated by Singular Value Decomposition (SVD), which allows identification of the geometric perturbation modes that are most *visible* in the far-field, and hence expected to be *reconstructible* in the inverse problem configuration.

Unlike traditional approaches which use global basis functions like *Karhunen-Loève* expansions [9, 6], the use of cubic splines allows for localised geometric perturbations, which is particularly valuable for understanding how specific geometric features influence the far-field. However, for such analysis it is paramount to be able to generate accurate numerical solutions, especially for complicated shapes with high spatial resolution. We overcome this by using the spectral *Nyström* method [2] for solving Boundary Integral Equations (BIEs), and we ensure the required smoothness of our scatterer's boundary representation.

In Section 2 we present the the class of scatterers considered in this article, Section 3 focuses on the wave scattering model including the governing BIEs that lead to the sensitivity matrix. In Section 4 we demonstrate our corresponding numerical results with focus on the SVD analysis. Conclusions

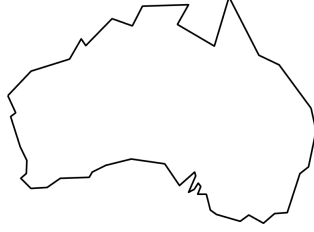


Figure 1: Visualisation of our reference scatterer, a polygonal approximation to the coast of mainland Australia.

are given in Section 5.

2 Scatterer representation: splines

Let $D(\boldsymbol{\omega}) \subset \mathbb{R}^2$ denote the simply connected region occupied by the scatterer, where $\boldsymbol{\omega}$ denotes a vector characterising the domain D . We assume that $D(\boldsymbol{\omega})$ is *star-shaped* with centre at the origin (see Fig 2), and use polar coordinates to parametrise $\partial D(\boldsymbol{\omega})$ through the continuous map $\boldsymbol{\chi} : [0, 2\pi) \rightarrow \partial D(\boldsymbol{\omega})$ given by

$$\boldsymbol{\chi}(\theta) = r(\theta)\hat{\mathbf{e}}_r(\theta), \quad \theta \in [0, 2\pi), \quad (1)$$

where $r(\theta) > 0$, and $\hat{\mathbf{e}}_r(\theta) = \cos \theta \hat{\mathbf{e}}_x + \sin \theta \hat{\mathbf{e}}_y$ represents the (unit) vector in the radial direction and $\hat{\mathbf{e}}_x, \hat{\mathbf{e}}_y$ are the constant Cartesian unit vectors. The closedness of the boundary implies that $\boldsymbol{\chi}(0) = \boldsymbol{\chi}(2\pi)$.

We are interested in a class of scatterers in which the *log-radius* $s(\theta)$, satisfying

$$r(\theta) = e^{s(\theta)}, \quad (2)$$

is a cubic spline utilising piecewise C^2 polynomials and periodic end conditions, so that

$$s(\theta) = \sum_{j=1}^{N_{\text{spline}}} a_j(\boldsymbol{\omega})(\theta - \theta_j^{\partial D})^3 + b_j(\boldsymbol{\omega})(\theta - \theta_j^{\partial D})^2 + c_j(\boldsymbol{\omega})(\theta - \theta_j^{\partial D}) + d_j(\boldsymbol{\omega}), \quad (3)$$

for $\theta \in [\theta_j^{\partial D}, \theta_{j+1}^{\partial D})$. The equispaced knots are $\theta_j^{\partial D} = 2\pi(j-1)/N_{\text{spline}}$ for $j = 1, \dots, N_{\text{spline}}$. In practice, the values $d_i \equiv s(\theta_i^{\partial D})$ for $i = 1, \dots, N_{\text{spline}}$ of the log-radius at the knots are sufficient to uniquely describe the scatterer, and without loss of generality we can write the vector of coefficients $\mathbf{d}(\boldsymbol{\omega}) = \boldsymbol{\omega} \in \mathbb{R}^{N_{\text{spline}}}$, and $\mathbf{a}(\boldsymbol{\omega}), \mathbf{b}(\boldsymbol{\omega}), \mathbf{c}(\boldsymbol{\omega})$ in (3) are obtained by solving an associated linear system where only the right hand side depends on $\boldsymbol{\omega}$. Scatterers obtained using the construction (3) for the shape in Figure 1 with $N_{\text{spline}} = 12, 48$ are depicted in Figure 2.

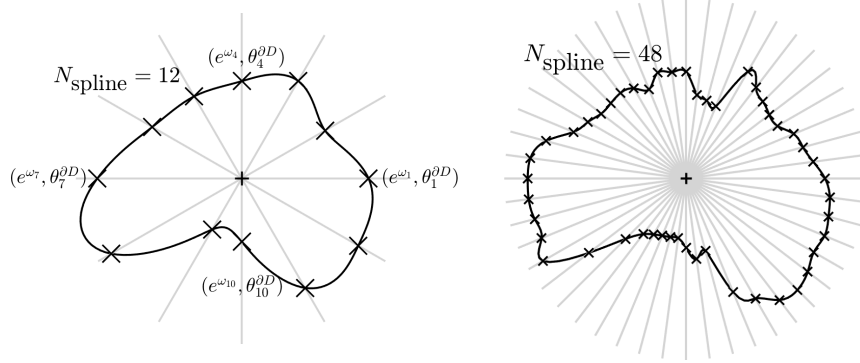


Figure 2: Star-shaped cubic spline scatterers D approximating the shape in Figure 1, for $N_{\text{spline}} = 12, 48$. The “+” symbol represents the scatterers center and the “x” visualise the knots and their associated data. The left plot includes reference $(r, \theta^{\partial D})$ boundary values.

3 Scattering model for sensitivity analysis

We consider time-harmonic waves with angular frequency ψ propagating in a non-dispersive homogeneous medium with constant wave speed c exterior to $D(\omega)$. The respective waves are described by the complex valued function $u(\mathbf{x}; \omega)$, which satisfies the 2D Helmholtz equation

$$(\Delta + k^2) u(\mathbf{x}; \omega) = 0, \quad \mathbf{x} \in \mathbb{R}^2 \setminus \overline{D}(\omega), \quad (4)$$

where $k = \psi/c$ is the wavenumber. The waves are forced by an *incident* plane wave

$$u^{\text{inc}}(\mathbf{x}) = e^{ik\mathbf{x} \cdot \hat{\mathbf{d}}}, \quad (5)$$

travelling in the direction of the (unit) vector $\hat{\mathbf{d}}$, which induces a *scattered* field u^{sc} . The scattered field must additionally satisfy the radiation condition [3],

$$\frac{\partial u^{\text{sc}}}{\partial \mathbf{x}}(\mathbf{x}; \omega) - ik u^{\text{sc}}(\mathbf{x}; \omega) = o\left(\frac{1}{\sqrt{|\mathbf{x}|}}\right), \quad \text{as } |\mathbf{x}| \rightarrow \infty, \quad (6)$$

uniformly with respect to direction $\hat{\mathbf{x}} = \mathbf{x}/|\mathbf{x}| = \hat{\mathbf{e}}_r(\theta) \in \partial B$, where $\partial B \subseteq \mathbb{R}^2$ denotes the set of all directions in the unit circle. The radiation condition (6) allows us to introduce the far-field pattern $u^\infty(\hat{\mathbf{x}}; \omega)$ induced as a result of the interaction of an incident plane wave with the particle $D(\omega)$ via

$$u^{\text{sc}}(\mathbf{x}; \omega) = \frac{e^{ik|\mathbf{x}|}}{\sqrt{|\mathbf{x}|}} \left(u^\infty(\hat{\mathbf{x}}; \omega) + O\left(\frac{1}{|\mathbf{x}|}\right) \right), \quad \text{as } |\mathbf{x}| \rightarrow \infty, \quad (7)$$

see e.g. (eqn 3.109 in [2]).

This work is motivated by the inverse problem in which far-field data is used to reconstruct the shape of the scatterer. For a fixed incident plane wave, it is convenient to introduce the far-field operator $\mathcal{F} : C([0, 2\pi)) \rightarrow C(\partial B)$ by

$$\mathcal{F}[r(\theta, \boldsymbol{\omega})] = u^\infty(\hat{\mathbf{x}}; \boldsymbol{\omega}), \quad (8)$$

which maps the boundary ∂D (defined using r) of the sound-soft scatterer onto the far-field pattern of the scattered wave. For a sound-soft scatterer with Dirichlet boundary conditions on the boundary $\partial D(\boldsymbol{\omega})$, we have

$$u(\mathbf{x}; \boldsymbol{\omega}) = f, \quad \text{for } \mathbf{x} \in \partial D(\boldsymbol{\omega}), \quad (9)$$

with $f = 0$.

An efficient way to evaluate \mathcal{F} when $f = 0$ is to use the BIE reformulation

$$(\mathcal{I} + 2\mathcal{K}' - ik\mathcal{S}) \left[\frac{\partial u}{\partial \mathbf{n}} \right] = 2 \frac{\partial u^{\text{inc}}}{\partial \mathbf{n}} - ik u^{\text{inc}}, \quad \mathbf{x} \in \partial D(\boldsymbol{\omega}), \quad (10)$$

where \mathcal{I} is the identity operator, \mathcal{S} is the single-layer potential, and \mathcal{K}' is the double-layer transpose potential [2]. The unknown in (10) is the physical-quantity $\partial u / \partial \mathbf{n}$, where $\mathbf{n}(\mathbf{x}_0)$ denotes the outward unit normal to $\partial D(\boldsymbol{\omega})$ at \mathbf{x}_0 . Once $\partial u / \partial \mathbf{n}$ has been computed by solving (10), we compute the scattered field away from the boundary as $u^{\text{sc}} = -\mathcal{S}[\partial u / \partial \mathbf{n}]$ for $\mathbf{x} \in \mathbb{R}^2 \setminus \overline{D}(\boldsymbol{\omega})$. The far-field can then be computed similarly.

We compute high-order approximate solutions to the wave-scattering problem introduced above using a spectral Nyström method, implemented in open source software [4], in which equation (10) is discretized using equispaced points on the boundary $\partial D(\boldsymbol{\omega})$, leading to a linear system

$$\mathbf{A}(\boldsymbol{\omega})\boldsymbol{\phi}(\boldsymbol{\omega}) = \mathbf{b}, \quad (11)$$

where the matrix $\mathbf{A}(\boldsymbol{\omega})$ represents the discretization of the combined field integral operators on the left hand side of (10), \mathbf{b} contains samples of the right hand side of (10) evaluated at the discretization points, and $\boldsymbol{\phi}$ approximates $\partial u / \partial \mathbf{n}$ at these points. We emphasise that, because the integration in (10) is over the boundary ∂D , the matrix $\mathbf{A}(\boldsymbol{\omega})$ must be recomputed for each new scatterer configuration.

Next we examine the sensitivity of the far field to changes in the scatterer's data, by considering the partial derivatives of the mapping $\mathcal{F} : r(\theta; \boldsymbol{\omega}) \mapsto u^\infty$. Using the chain rule gives

$$J_i = \frac{\partial \mathcal{F}}{\partial \omega_i} = \frac{d\mathcal{F}}{dr} \left[\frac{\partial r}{\partial \omega_i} \right], \quad \frac{\partial r}{\partial \omega_i} = r(\theta) \frac{\partial s(\theta; \boldsymbol{\omega})}{\partial \omega_i}. \quad (12)$$

Here $d\mathcal{F}[\cdot]/dr$ is the *Fréchet derivative* of \mathcal{F} . The Fréchet derivative is given by the far-field of an auxiliary wave field v satisfying (4), (6) and the inhomogeneous Dirichlet condition (see [2, Theorem 5.15])

$$v(\mathbf{x}; \boldsymbol{\omega}) = -\mathbf{n} \cdot (q(\theta)\hat{\mathbf{e}}_r(\theta) \circ \boldsymbol{\chi}^{-1}) \frac{\partial u}{\partial \mathbf{n}} \quad \text{for } \mathbf{x} \in \partial D(\boldsymbol{\omega}), \quad (13)$$

with $q \in \partial B$ a scalar function representing the direction. To compute v we solve the combined-field BIE [2, (3.29)] for ϕ^* where the inhomogeneity is coupled with (10),

$$(\mathcal{I} + 2\mathcal{K} + 2ik\mathcal{S})[\phi^*] = -2\mathbf{n} \frac{\partial u}{\partial \mathbf{n}} \cdot (q(\theta)\hat{\mathbf{e}}_r(\theta) \circ \boldsymbol{\chi}^{-1}), \quad \mathbf{x} \in \partial D(\boldsymbol{\omega}). \quad (14)$$

Once the surface potential ϕ^* has been obtained by solving (14), we compute the induced field using $v(\mathbf{x}) = (\mathcal{K} + ik\mathcal{S})[\phi^*]$ for $\mathbf{x} \in \mathbb{R}^2 \setminus \overline{D}(\boldsymbol{\omega})$. The far field is computed similarly.

Remark 1. We use the BIE (10) to solve the forward scattering problem because it yields the surface potential $\partial u / \partial \mathbf{n}$, which is required in the right hand side of (14) to compute the Fréchet derivative. The BIE (10) is not appropriate for solving the Fréchet-derivative PDE subject to the Dirichlet data in (13), because the right hand side of (10) would require a further normal derivative of u ; in this case the simpler indirect BIE (14) is preferred.

To better understand the sensitivity of the derivative to perturbations in the shape, we compute the singular value decomposition

$$|\mathbf{J}| = \mathbf{U}\boldsymbol{\Sigma}\mathbf{V}^\top, \quad (15)$$

where $J_{ij} = J_i(\theta_j)$ are the entries in the Jacobian matrix, $\boldsymbol{\Sigma}$ is the matrix of singular values $\sigma_i \geq 0$, $\mathbf{U} = [\mathbf{u}_1 | \mathbf{u}_2 | \dots | \mathbf{u}_{N_{\text{spline}}}]$, with \mathbf{u}_i the unit left singular vectors and $\mathbf{V} = [\mathbf{v}_1 | \mathbf{v}_2 | \dots | \mathbf{v}_{N_{\text{obs}}}]$ with \mathbf{v}_i the (unit) right singular vectors of $|\mathbf{J}|$. For multiple incident waves we define \mathcal{F} to be the concatenation of the mappings for each incident wave. Then an analogue of (15) applies and $|\mathbf{J}| \in \mathbb{R}^{N_{\text{spline}} \times (N_{\text{inc}} N_{\text{obs}})}$ is the reshaped sensitivity matrix including all incident directions. This is useful since, as we will see below, it deemphasises the role of the incident wave direction in identifying the most significant geometric features contributing to the far-field.

4 Numerical results

We present results for the scatterers in Figure 2 with $N_{\text{spline}} = 12, 48$. From (3), it can be seen that the the input function $q = \partial r / \partial \omega_i$ to the Fréchet operator

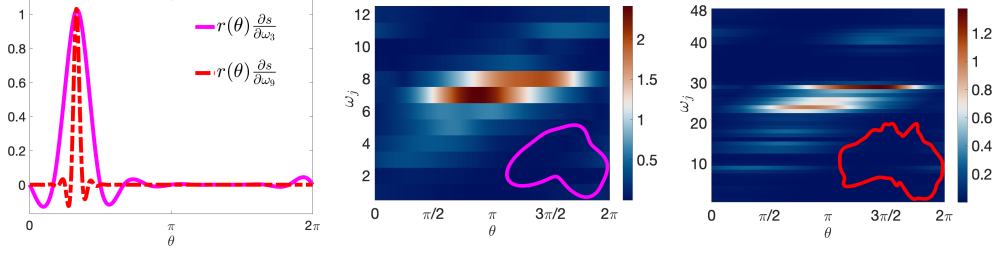


Figure 3: Left: Input function to the Fréchet operator (12) for our 2 scatterers at $\theta_i^{\partial D} = \pi/3$. Jacobian matrix $|\mathbf{J}|$ for $\hat{\mathbf{d}} = \hat{\mathbf{e}}_x$ for $ka = 2\pi$, $N_{\text{spline}} = 12$ (center) and $N_{\text{spline}} = 48$ (right).

(12) is itself a cubic spline whose values at the knots are $\partial s(\theta_i^{\partial D}; \boldsymbol{\omega})/\partial \omega_i = \mathbf{e}_i$. It follows that the associated perturbation of the shape is localised around ω_i , as is illustrated in Figure 3 (left).

We let a be the diameter of the smallest ball circumscribing the scatterer and present our results in terms of the non-dimensional frequency ka . Figure 3 (center, right) visualise the Jacobian matrix for a single incident wave with direction $\hat{\mathbf{d}} = \hat{\mathbf{e}}_x$ and $ka = 2\pi$. Here we use $N_{\text{obs}} = 1000$ and $N_{\text{Nys}} = 27, 240$ for $N_{\text{spline}} = 12, 48$ respectively, with the higher order quadrature required in the latter case to resolve the more complex geometry. These Jacobian plots contain key physical information, but the interplay between incident direction, observation angle, and geometric features makes interpretation challenging. We focus on these effects below making use of (15).

Next we consider the case of 4 incident waves with $\hat{\mathbf{d}} = \pm \hat{\mathbf{e}}_x, \pm \hat{\mathbf{e}}_y$. In Figures 4, 5 we visualise the left (shape) and right (far-field) singular vectors for the largest three singular values for $ka = 2\pi, 4\pi, 6\pi$ respectively. We note that increasing ka dictates a slower rate of decay of the singular values. We visualise the shape singular vectors $|\mathbf{u}_i|$ using colour on the scatterer boundary. For the far-field singular vectors $|\mathbf{v}_i|$ visualisation, we plot the associated acoustic cross section $|\mathbf{v}_i|^2$ in polar coordinates. Since we have 4 incident waves, there are 4 associated cross sections, discriminated by color. The far-field singular vectors are normalised by σ_i so that the size of the perturbation in the far field for a given shape perturbation can be quantified. For example, in the top right plots of both figures the far field is close to zero (the inner circle) indicating that the far field is not very sensitive to the third singular shape-vector.

These modes provide insight into which boundary features are most visible from far-field data across all incident waves. The most noticeable feature

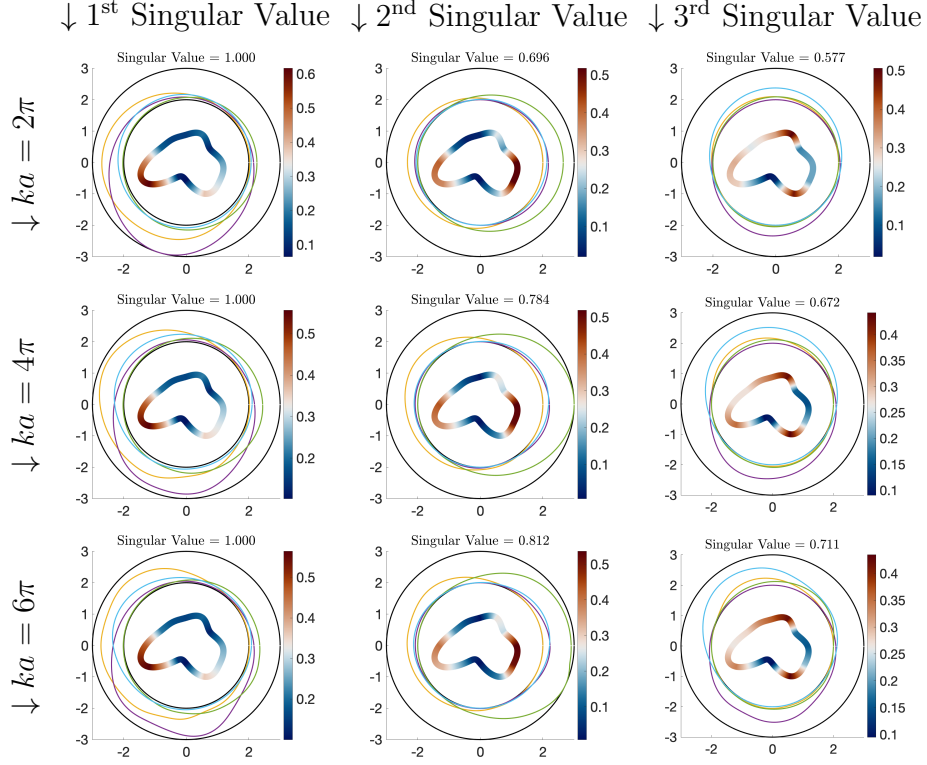


Figure 4: Visualisation of the first 3 singular values and associated right and left singular vectors for $N_{\text{spline}} = 12$ and $|\mathbf{J}|$ comprising of 4 incident waves with $\hat{\mathbf{d}} = \pm\hat{\mathbf{e}}_x, \pm\hat{\mathbf{e}}_y$.

is that the support of the first singular shape-vector is in all cases associated with the south-western tip of Western Australia. The corresponding singular far-field vectors show that this feature produces large perturbations in the far field for those incident waves that illuminate it.

All rows of Figure 4 show considerable sensitivity across the boundary except for the concave region in the southern tip corresponding to $\theta_{10}^{\partial D}$. In turn, this means that under these conditions, two scatterers that are identical except for small deviations in ω_{10} may have indistinguishable far-fields patterns, manifesting ill-posed behaviour. In Figure 5 the situation is significantly more complex, with many more identifiable regions with small sensitivity. This is nevertheless expected, since the finer details in the scatterer would require much higher ka values due to the *diffraction limit*.

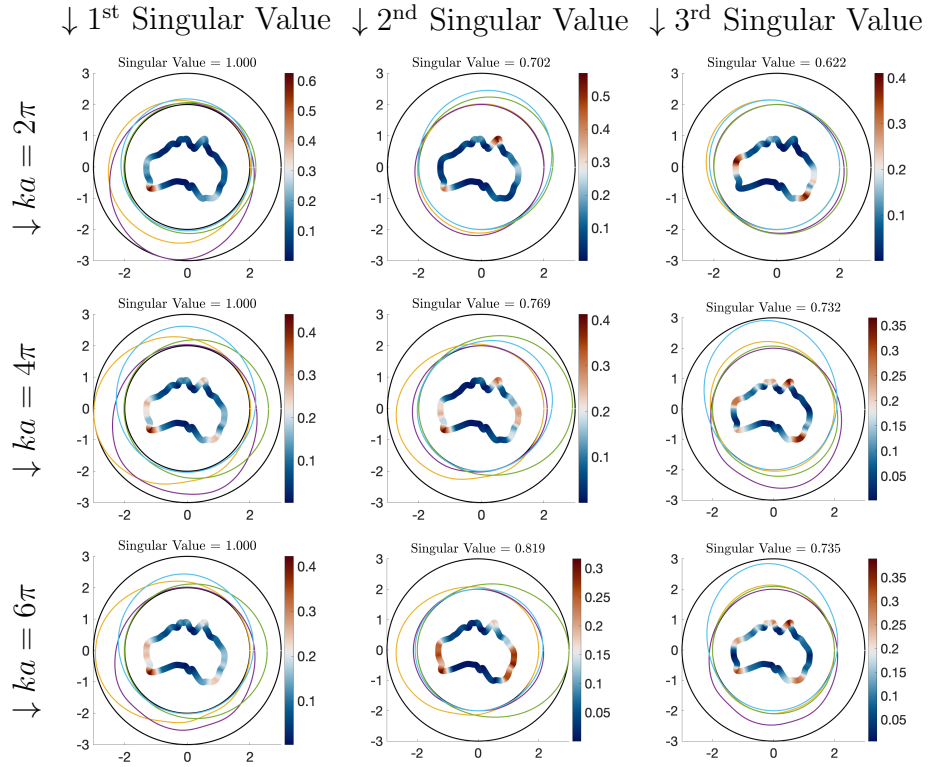


Figure 5: Visualisation of the first 3 singular values and associated right and left singular vectors for $N_{\text{spline}} = 48$ and $|\mathbf{J}|$ comprising of 4 incident waves with $\hat{\mathbf{d}} = \pm \hat{\mathbf{e}}_x, \pm \hat{\mathbf{e}}_y$.

5 Conclusions

We have provided an investigation of the effects of local perturbations to a given 2D scatterers shape in corresponding far-field patterns. These effects can be written in terms of the Fréchet derivative of the far-field operator $d\mathcal{F}[\cdot]/dr$ with N_{spline} localised input functions following from a splines representation for the scatterer. The computation reduces to a coupled BIE which is accurately solved using the Nyström method. Upon choosing observation directions, all results can be represented through a sensitivity matrix \mathbf{J} which we show can conveniently be studied using its SVD. This tool gives us instant useful information into the ill-posedness of the inverse problem such as which shape deformations can be reliably recovered from far-field data and, on the contrary, which are effectively invisible to far-field measurements.

References

- [1] Born, M. and Wolf, E. (2013). *Principles of optics: electromagnetic theory of propagation, interference and diffraction of light*. Elsevier.
- [2] Colton, D. and Kress, R. (2019). *Inverse acoustic and electromagnetic scattering theory* (4th ed.). Springer. doi: 10.1007/978-3-030-30351-8.
- [3] Schot, S. H. (1992). Eighty years of Sommerfeld’s radiation condition. *Historia mathematica*, 19(4), 385–401. Elsevier.
- [4] Ganesh, M. and Hawkins, S. C. (2017). Algorithm 975: TMATROM—a T-matrix reduced order model software. *ACM Transactions on Mathematical Software (TOMS)*, 44(1), 1–18. ACM New York, NY, USA.
- [5] Ganesh, M. and Hawkins, S. C. (2014). Scattering by stochastic boundaries: hybrid low-and-high-order quantification algorithms. *ANZIAM Journal*, 56, C312–C338.
- [6] Ganesh, M., Hawkins, S. C., Kordzakhia, N., and Unicomb, S. (2020). An efficient Bayesian neural network surrogate algorithm for shape detection. *ANZIAM Journal*, 62, C112–C127.
- [7] Borges, C. and Rachh, M. (2022). Multifrequency inverse obstacle scattering with unknown impedance boundary conditions using recursive linearization. *Advances in Computational Mathematics*, 48(1), 2. Springer.

- [8] Ganesh, M. and Hawkins, S. C. (2011). A fully discrete Galerkin method for high frequency exterior acoustic scattering in three dimensions. *Journal of Computational Physics*, 230(1), 104–125. Elsevier.
- [9] Yang, Z., Gui, X., Ming, J., and Hu, G. (2021). Bayesian approach to inverse time-harmonic acoustic obstacle scattering with phaseless data generated by point source waves. *Computer Methods in Applied Mechanics and Engineering*, 386, 114073. Elsevier.